Journal of Nuclear Materials 556 (2021) 153198

Contents lists available at ScienceDirect

Journal of Nuclear Materials

journal homepage: www.elsevier.com/locate/jnucmat

Synthesis of $Ca_{1-x}Ce_xZrTi_{2-2x}Al_{2x}O_7$ zirconolite ceramics for plutonium disposition ☆

Min-Xiao Zhong[a,b], Brant Walkley[b,c], Daniel J. Bailey[b], Lewis R. Blackburn[b], Hao Ding[b], Shi-Qian Wang[a], Wei-Chao Bao[d], Laura J. Gardner[b], Shi-Kuan Sun[b,e,*], Martin C. Stennett[b], Claire L. Corkhill[b], Neil C. Hyatt[b]

[a] Science and Technology on Reactor System Design Technology Laboratory, Nuclear Power Institute of China, Chengdu, Sichuan 610041, China
[b] Immobilisation Science Laboratory, Department of Materials Science and Engineering, University of Sheffield, Sheffield S1 3JD, United Kingdom
[c] Department of Chemical and Biological Engineering, University of Sheffield, Sheffield S1 3JD, United Kingdom
[d] The State Key Laboratory of High Performance Ceramics and Superfine Microstructure, Shanghai Institute of Ceramics, Chinese Academy of Sciences, Shanghai 200050, China
[e] School of Material Science and Energy Engineering, Foshan University, Guangdong 528000, China

ARTICLE INFO

Article history:
Received 6 May 2021
Revised 14 July 2021
Accepted 16 July 2021
Available online 19 July 2021

Keywords:
Plutonium immobilisation
Ceramic wasteforms
Zirconolite
Waste loading
Local environment

ABSTRACT

A series of zirconolite ceramics with stoichiometry $Ca_{1-x}Ce_xZrTi_{2-2x}Al_{2x}O_7$ (x = 0–0.35), considered as a host phase for the immobilisation of separated plutonium, were prepared from a mixture of oxide precursors by sintering in air at 1450 °C. Ce was utilised as a structural surrogate for Pu, with Al added to provide charge compensation. XRD and electron diffraction analyses indicated crystallisation of the zirconolite-2M polytype for all compositions, accompanied by various secondary phases contingent on the doping level, consistent with microstructure observation. The relative yield of zirconolite phases remained above 94 wt.% for $0.05 < x < 0.20$. It was determined that Ce was partially reduced to the Ce^{3+} oxidation state and Al occupied mainly octahedral Ti sites. The incorporation rate of CeO_2 was calculated to be 9.27 wt.% in $Ca_{0.80}Ce_{0.20}ZrTi_{1.60}Al_{0.40}O_7$ with a comparatively high yield of 94.7 wt.%, which is representative of a PuO_2 incorporation rate of 14.86 wt.%.

1. Introduction

The United Kingdom currently holds the world's largest inventory of separated plutonium, under civil safeguards, with an inventory of over 140 t forecast at the end of reprocessing options [1,2]. Current UK government policy is to reuse this separated plutonium as MOX fuel in light water reactors. However, an alternative option currently under consideration is immobilisation of plutonium within a chemically durable wasteform and disposal in an engineered geological disposal facility [3]. Titanate ceramics are a family of crystalline materials that are under development as hosts for high level radioactive waste streams due to superior aqueous durability with respect to vitrified wasteforms [4–6].

Zirconolite, prototypically $CaZrTi_2O_7$, has been proposed as a potential candidate for immobilising Pu due to its excellent chemical durability and radiation tolerance [7,8]. Natural zirconolites have been found to contain up to 20 wt.% of uranium and thorium with ages in excess of a billion years [9]. Although some natural analogues have become metamict (amorphised) due to the effects of self-irradiation, the fact that they have retained significant quantities of U/Th is promising with regards to the long-term stability of zirconolite as the advanced ceramic wasteform for actinides. Zirconolite has the general formula $CaZr_xTi_{3-x}O_7$ that crystallises in 2M polytype, in the space group C2/*c*, over the compositional range $0.8 \leq x \leq 1.37$ [10]. The crystal structure of zirconolite-2M, demonstrated in Fig. 1, is considered as a derivative of the well known pyrochlore structure (space group: Fd-3*m*) [10,11]. Distortion perpendicular to the (111) plane of the pyrochlore structure results in the monoclinic (C2/*c*) zirconolite-2M structure, consisting the hexagonal tungsten bronze layers perpendicular to the [001] direction. The Ca and Zr cations are 8- and 7- fold co-ordinate,

☆ Dedication: In memorium, Dr Eric (Lou) Vance, 15 November 1942–7 March 2019, latterly Chief Scientist, Australian Nuclear Science and Technology Organization.

* Corresponding author at: Immobilisation Science Laboratory, Department of Materials Science and Engineering, University of Sheffield, Sheffield S1 3JD, United Kingdom
E-mail address: shikuan.sun@sheffield.ac.uk (S.-K. Sun).

https://doi.org/10.1016/j.jnucmat.2021.153198

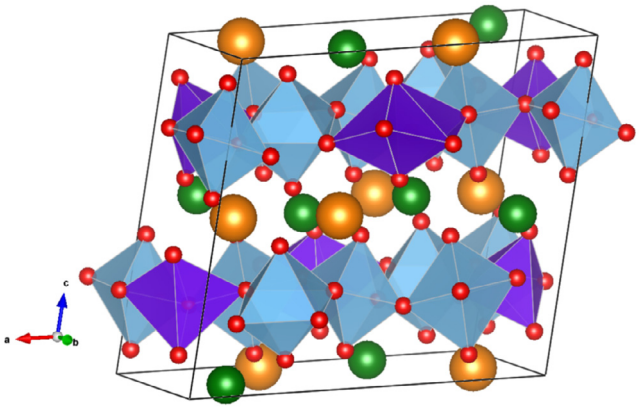

Fig. 1. Structural model of zirconolite-2M phase (C2/*c*). Ca atom in orange, Zr atoms in green, TiO_6 polyhedra in light blue, TiO_5 polyhedra in purple (For interpretation of the references to color in this figure legend, the reader is referred to the web version of this article.).

respectively. Three unique Ti co-ordination polyhedral form, comprising two fully occupied octahedral sites (light blue TiO_6 polyhedra in Fig. 1) and a 50% occupied trigonal bi-pyramidal site (TiO_5 in Fig. 1) [11]. In principle, actinides such as Pu^{4+} are capable of entering the zirconolite lattice *via* solid solution with (i) Ca site whilst ions such as Al^{3+} can occupy Ti sitesin formulations that do not exhibit aliovalence, or (ii) Zr site without charge compensator. Begg et al. attempted co-substitution of Pu/Np within zirconolite and deduced that whilst Pu could be accepted within solid solution, Pu valence was dependent on the processing atmosphere [12].

Laboratory studies of Pu containing materials require dedicated facilities and specialist handling equipment due to the hazards associated with Pu. As a result, experiments utilising plutonium are expensive and hazardous, hence the use of inactive/less hazardous structural surrogates is commonplace in early stage formulation research. Ce is often used as a surrogate for Pu due to similarities in oxidation state (trivalent and tetravalent) and ionic radii (e.g. Ce^{4+} = 0.97 Å and Pu^{4+} = 0.96 Å in eightfold coordination) [13]. In this study, Ce^{4+} from CeO_2 is utilised to simulate Pu^{4+} in PuO_2, mainly arising from reprocessing plants. Blackburn et al. found that the mixture of zirconolite-2M and zirconolite-4M polytypes, alongside secondary perovskite phases, was produced when heating $CaZr_{0.8}Ce_{0.2}Ti_2O_7$ in air [14]. For the Ca-site substitution, Vance *et al.* prepared zirconolites of $Ca_{0.8}Ce^{3+}{}_{0.2}ZrTi_{1.8}Al_{0.2}O_7$ and $Ca_{0.8}Ce^{4+}{}_{0.2}ZrTi_{1.6}Al_{0.4}O_7$ by hot-pressing and sintering, Al^{3+} was added as a charge compensating species to maintain charge neutrality [15]. The Ca site was replaced by Ce^{3+} or Ce^{4+} as the target stoichiometry in both cases and pure zirconolite was obtained for $Ca_{0.8}Ce^{3+}{}_{0.2}ZrTi_{1.8}Al_{0.2}O_7$, while zirconolite was the major phase for $Ca_{0.8}Ce^{4+}{}_{0.2}ZrTi_{1.6}Al_{0.4}O_7$ with minor amount of Al_2O_3 [15]. However, the graphite-rich environment during hot-pressing would provide a naturally reducing environment, making the inherent redox behaviour of Ce in zirconolite difficult to understand.

In this study, a suite of Ce-Al co-doped zirconolites, formulated $Ca_{1-x}Ce_xZrTi_{2-2x}Al_{2x}O_7$ (x = 0–0.35), were synthesised in air using Ce as a structural surrogate for Pu. The current work aims to develop the fundamental understanding of the solid solution behaviour of zirconolite wasteforms in part with charge compensating species. This understanding would contribute essential underpinning evidence to support any future change in UK government policy for plutonium inventory management, to adopt immobilisation and disposal in the form of a ceramic zirconolite wasteform [16]. On this basis, the phase assemblage, polymorphic behaviour, chemical composition, the crystal structure and the redox behaviour of Ce in the sintered zirconolites were investigated as a function of Ce incorporation, from which we aim to draw an inference for Pu immobilisation behaviour when using Al^{3+} as a charge compensating species.

2. Materials and methods

2.1. Zirconolite fabrication

The reagents used in this study were: $CaTiO_3$ (Alfa Aesar, purity ≥ 99.0 %), CeO_2 (Acros Organics, ~ 99.9%), ZrO_2 (Aldrich, ~ 99.0%), Al_2O_3 (Alfa Aesar, ~ 99.7%) and TiO_2 (Aldrich, ≥ 99.0 %). The oxide precursors were batched with a target composition of $Ca_{1-x}Ce_xZrTi_{2-2x}Al_{2x}O_7$ (x = 0–0.35; Δx = 0.05) and mixed by planetary milling with acetone and Si_3N_4 ball media. The mixtures were dried and cold-pressed under the pressure of 100 MPa. All specimens were sintered in air at 1450 °C for 12 h, with ramping and cooling rates of 5 °C/min.

2.2. Phase and microstructural characterisation

Reacted samples were ground and characterised by powder X-ray diffraction (PXRD, D2 Phaser Diffractometer, Bruker; Cu-K_α) in the range 10 ° ≤ 2θ ≤ 110 ° with step size of 0.02 °. Refinement of PXRD patterns were performed to calculate the lattice parameter and weight fraction using the GSAS software package [17], with LaB_6 used as the internal standard. Samples for microstructure observation were polished to a 1.0 µm optical finish using progressively finer SiC paper and diamond pastes. Hitachi TM3030 scanning electron microscope (SEM) was used for observation of the polished surface and energy-dispersive X-ray spectroscopy analysis (EDX) was performed using a Quantax 70 (Bruker) system coupled with SEM. The semi quantitative cation composition was determined based on 20 EDX data points.

2.3. Local environment analysis

Transmission mode Ce L_3 Edge X-ray Absorption Near Edge Structure (XANES) data were acquired using an EasyXAFS XES 100-extended spectrometer, using the (4 2 2) harmonic of a Si (2 1 1) spherically bent crystal analyser (for a Rowland circle of 1 m diameter), to monochromate the Bremsstrahlung radiation of a Pd X-ray tube operating at 25 kV and 4 mA [18–20]. A helium beam path was maintained to minimise X-ray attenuation. Data were acquired with a step size of 0.50 eV in the XANES region (5700–5900 eV) and a count time of 10 s per step. Data were acquired sequentially in the absence of a sample (I_0) and in the presence of a sample (I_t), using a Hitachi Vortex silicon drift detector. Data were normalised, aligned to the absolute energy scale (calibrated by a Cr foil), summed, and background subtracted using the Athena program [21]. Data were also acquired on $CePO_4$ (monazite) and CeO_2 reference compounds, characteristic of Ce^{3+} and Ce^{4+} respectively. XANES samples were prepared to yield an edge step of *ca.* $\mu_x = 1$, by dilution of the required quantity of material in polyethylene glycol and pressing as 13 mm diameter pellet. Linear combination fitting of the XANES data from the reference compounds to that of $Ca_{1-x}Ce_xZrTi_{2-2x}Al_{2x}O_7$, over the range 5680–5760 eV, under the constraint that the fractional weights of the reference spectra summed to unity.

Solid state single pulse ^{27}Al magic angle spinning (MAS) nuclear magnetic resonance (NMR) spectra of the powdered $Ca_{1-x}Ce_xZrTi_{2-2x}Al_{2x}O_7$ (x = 0.05–0.35) samples were acquired using a Bruker Avance III HD 500 spectrometer at 11.7 T (B_0) using a 4.0 mm dual resonance CP/MAS probe, yielding a Larmor frequency of 130.32 MHz. Spectra were acquired using a 1.4 μs non-selective ($\pi/2$) excitation pulse, a measured 60 s relaxation delay, a total of 64 scans and spinning at 12.5 kHz. All spectra

were referenced to 1.0 M aqueous $Al(NO_3)_3$ at 0 ppm. Due to the existence of the hibonite phase, NMR data of hibonite (prepared by solid state reaction) was also collected for comparison. Selected area electron diffraction (SAED) patterns were acquired for a sample with a target composition of $Ca_{0.75}Ce_{0.25}ZrTi_{1.5}Al_{0.5}O_7$, using a JEM 2100F (JEOL) transmission electron microscope (TEM), operating at 200 keV. Powdered sample after grinding was dispersed with acetone and pipetted onto the Cu-grid (Agar) for TEM analysis.

3. Results and discussion

All compositions were characterised by powder X-ray diffraction (Fig. 2). Reflections of zirconolite-2M (space group: C2/*c* [22]) were observed for all compositions, as shown in Fig. 2A. No reflections corresponding to CeO_2 were observed, indicative of complete incorporation within the ceramic wasteform. Compositions within range $0 \leq x \leq 0.15$ were found to contain a small amount of perovskite (prototypically, $CaTiO_3$), characterised by the weak (112) reflection at $2\theta = 33.2^{\circ}$. As displayed in Fig. 2B, increasing the Ce incorporation rate to $x \geq 0.20$, resulted in the formation of secondary hibonite ($CaAl_{12}O_{19}$, PDF #84–1613[23]) and the retention of corundum (Al_2O_3). These results are indicative that the co-doping of Ce and Al within the zirconolite structure was achieved within the range $0 < x \leq 0.15$.

Rietveld fitting of PXRD data was performed to determine the lattice parameters of synthesised zirconolites, see Table 1. Fig. S1 (see *Supporting Information*) presents representative Rietveld fits of the $x = 0.15$ and $x = 0.25$ compositions. The refined lattice parameters of $CaZrTi_2O_7$ ($x = 0$) were in good agreement with those reported by Whittle et al. [22] It was observed that *a* and β gradually increased as Ce and Al doping was increased from $x = 0.05$, whereas *b* and *c* remained almost constant. Quantitative phase analysis (Fig. 3) found that the weight fraction attributed to perovskite remained $\leq$ 3.1% for compositions with $0 \leq x \leq 0.15$. Perovskite did not appear as a secondary phase when higher levels of Ce substitution (≥ 0.20) were targeted. The weight fraction of Al_2O_3 and $CaAl_{12}O_{19}$ phases increased to 13.5 wt.% and 1.6 wt.%, respectively, for the composition with $x = 0.25$, increasing to 16.3 wt.% and 7.4 wt.%, for $x = 0.35$. It may be inferred that the substitution limit of Ce/Al is $x = 0.20$ for $Ca_{1-x}Ce_xZrTi_{2-2x}Al_{2x}O_7$, as evidenced by the marked increase in secondary phase formation at higher levels of attempted substitution.

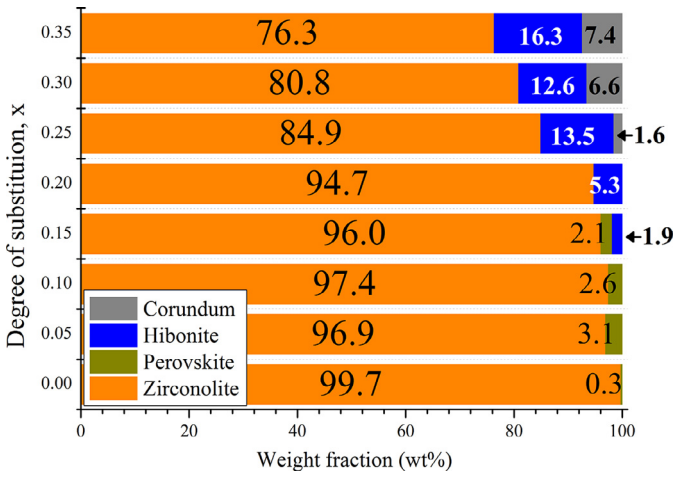

Fig. 3. Quantitative phase analysis results in the $Ca_{1-x}Ce_xZrTi_{2-2x}Al_{2x}O_7$ system as a function of composition.

SEM images of the synthesised zirconolites are shown in Fig. 4. All compositions exhibited a dense microstructure with little observable porosity (below ~ 5%). The zirconolite grain size was typically found to lie in the range of 10–20 μm. When low Ce incorporation was targeted, $0.05 < x < 0.15$, zirconolite (denoted by *Z* in Fig. 4) was observed as the dominant phase, consistent

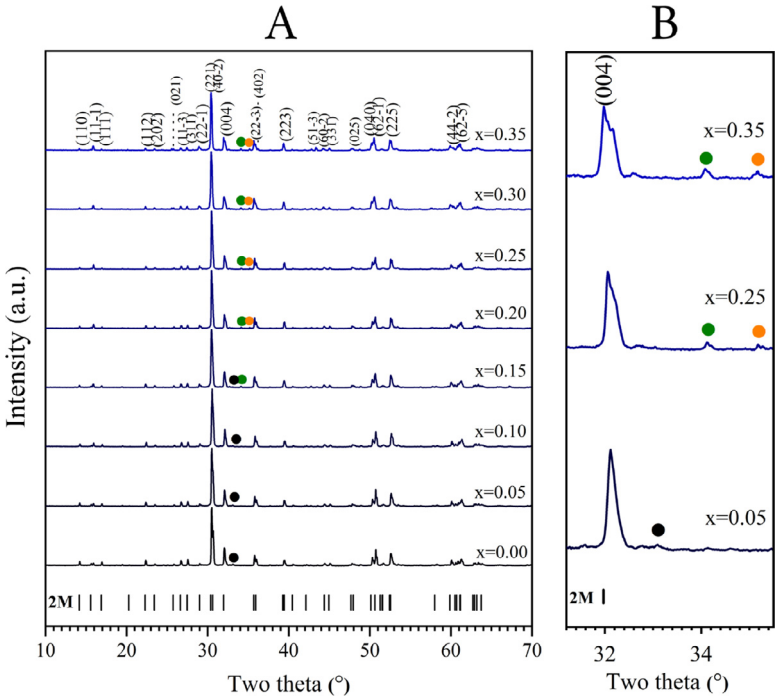

Fig. 2. (A) Powder XRD patterns of Ce-Al co-doped zirconolite with composition $Ca_{1-x}Ce_xZrTi_{2-2x}Al_{2x}O_7$ after sintering in air at 1450°C for 12 h; vertical marks show allowed reflections of zirconolite-2M.[22] (B) The enlargement inset shows the existence of the secondary phases. Perovskite reflections are labelled by black circles; $CaAl_{12}O_{19}$ and Al_2O_3 are labelled by green circles and orange circles (For interpretation of the references to color in this figure legend, the reader is referred to the web version of this article.).

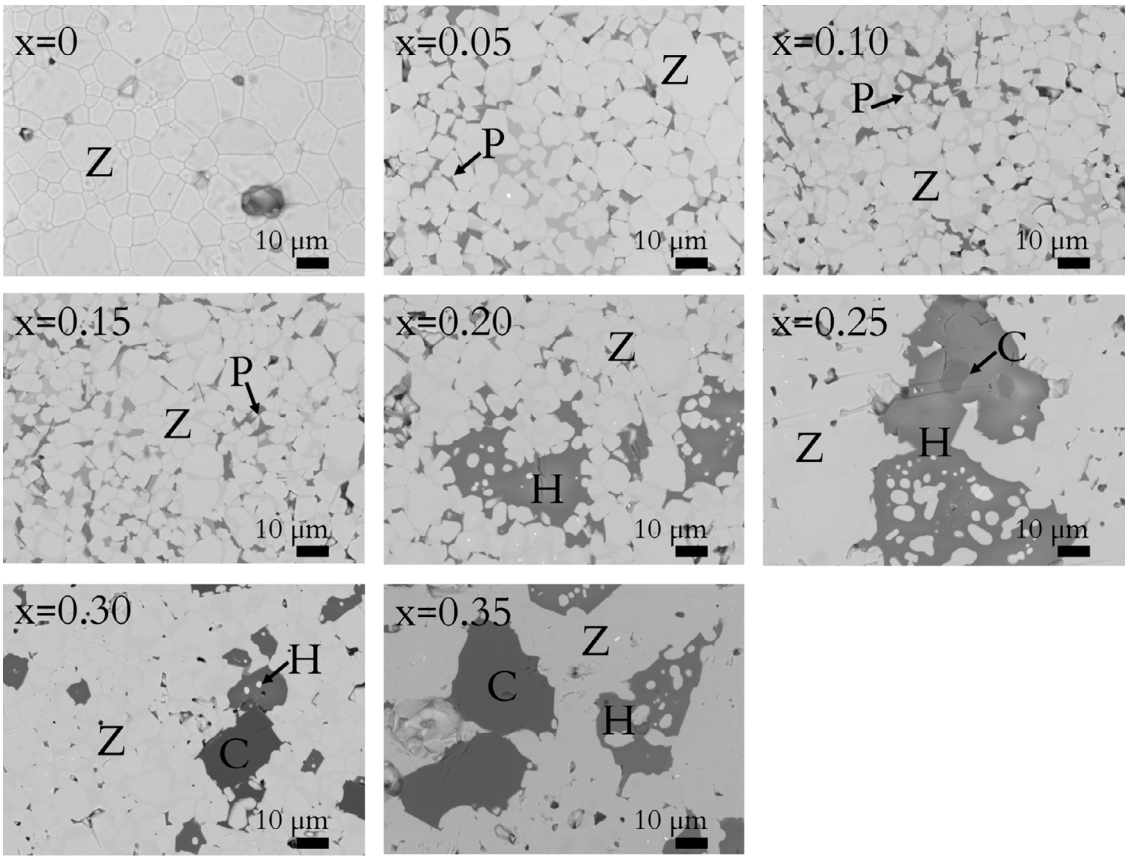

Fig. 4. Representative SEM observation of the polished samples. **Z**–Zirconolite, **P**–Perovskite, **H**–Hibonite and **C**–Corundum.

with PXRD data. Perovskite (P) was clearly present as a secondary phase and appeared to form at zirconolite grain boundaries. The microstructure of compositions with higher targeted Ce concentration (*i.e.* $x \geq 0.20$) contained large inclusions of dark contrast identified as $CaAl_{12}O_{19}$ (H-hibonite) and Al_2O_3 (C-corundum). The relative fraction of these phases within the microstructure increased as a function of doping, in agreement with quantitative phase analysis obtained from refinement of PXRD. EDX analysis for the zirconolite sample with target stoichiometry $Ca_{0.75}Ce_{0.25}ZrTi_{1.5}Al_{0.5}O_7$ ($x = 0.25$) is shown in Fig. 5; analysis of elemental distribution (Table 2 and Table S1 in *Supporting Information*) confirmed the formation of the hibonite phase and retention of Al_2O_3. Notably, Ce was observed to be overwhelmingly incorporated in the zirconolite phase, only trace Ce incorporation within the perovskite phase ($x = 0.05$–0.15) and hibonite phase ($x = 0.15$–0.35) was evident from EDX analysis.

Ce L_3 edge XANES data of the zirconolite samples are shown in Fig. 6. By comparison with data from the CeO_2 standard, the XANES features of the zirconolite composition are consistent with the majority of Ce being speciated as Ce^{4+}. However, a proportion of the Ce speciation was present as Ce^{3+}, which is indicated by the shift to lower energy of E_0 (*e.g.* $\Delta E \approx 1.0$ eV for $x = 0.20$ when comparing with CeO_2) and increased intensity in the immediate post edge feature. Derived from linear combination fitting of XANES spectra (see Fig. S2 in *Supporting Information*), the fraction of Ce^{3+} was observed to increase (Table 2) concurrently with Ce incorporation (x) in the products. The existence of trivalent Ce (Ce^{3+}) was previously reported when incorporating Ce in the hibonite and perovskite structured compounds [24,25]. Assuming trace Ce incorporated within the hibonite and perovskite phases occurred as Ce^{3+}, the ratio of Ce^{3+}/Ce^{4+} for zirconolite phase could be derived, as reported in Table 2. The ratio of Ce^{4+} speciation to (Ce^{3+} + Ce^{4+}) in the zirconolite phase gradually decreased as the substitution level was increased. Due to the formation of Al_2O_3 and $CaAl_{12}O_{19}$ phases, the incorporation of Al in the zirconolite phase was below the nominal target concentration; therefore, the

Table 1
Refined structural parameters for $Ca_{1-x}CexZrTi_{2-2}xAl2xO7$ ($0.00 \leq x \leq 0.35$) determined from Rietveld analysis of powder X-ray diffraction data.

Composition	*a* (Å)	*b* (Å)	*c* (Å)	*β* (°)	*V* (Å^3)	R_p (%), R_{wp} (%), χ^2
$x = 0.00$	12.4429(4)	7.2722(2)	11.3764(4)	100.570(3)	1011.95(4)	7.69, 6.09, 2.856
$x = 0.05$	12.4325(5)	7.2505(3)	11.3618(5)	100.610(3)	1006.66(5)	7.63, 5.70, 3.173
$x = 0.10$	12.4379(6)	7.2470(3)	11.3526(5)	100.643(6)	1005.70(6)	8.68, 6.41, 4.122
$x = 0.15$	12.4421(7)	7.2459(4)	11.3497(6)	100.658(6)	1005.58(7)	7.96, 6.07, 3.321
$x = 0.20$	12.4507(8)	7.2490(4)	11.3500(7)	100.678(6)	1006.66(8)	8.35, 6.41, 3.861
$x = 0.25$	12.4582(8)	7.2501(4)	11.3587(7)	100.674(6)	1008.20(8)	9.95, 7.56, 5.655
$x = 0.30$	12.4798(10)	7.2572(5)	11.3630(9)	100.720(9)	1011.16(10)	8.73, 6.86, 4.058
$x = 0.35$	12.4881(18)	7.2599(11)	11.3686(15)	100.739(12)	1012.65(35)	9.78, 7.54, 4.857

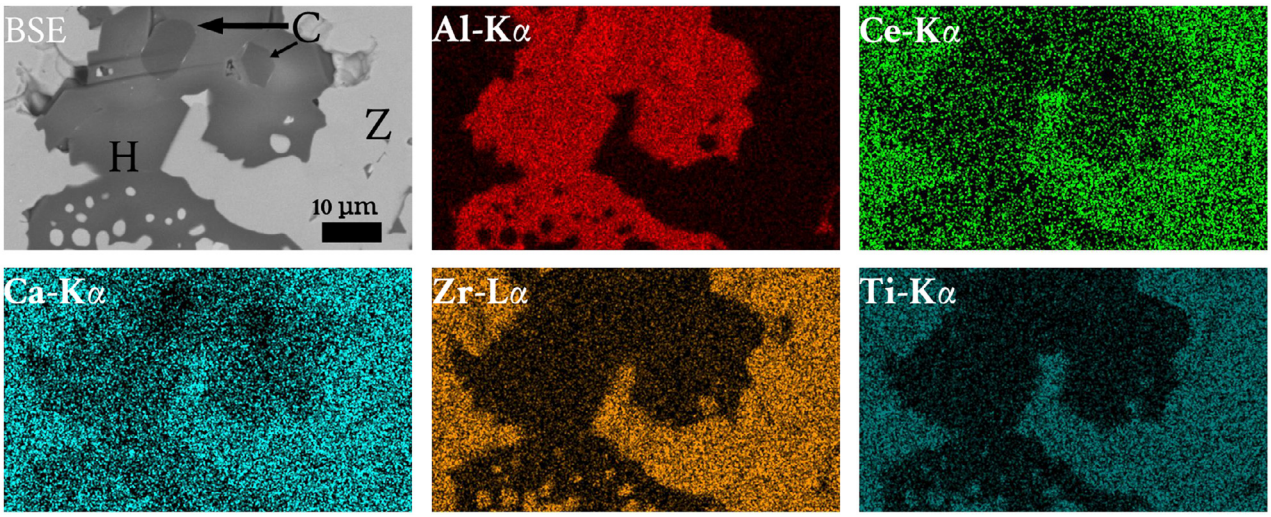

Fig. 5. Elemental partitioning of $Ca_{0.75}Ce_{0.25}ZrTi_{1.5}Al_{0.5}O_7$ samples. **Z**–Zirconolite, **H**–Hibonite and **C** – Corundum.

Table 2
Weight fraction, ratio of $Ce^{3+/4+}$ and chemical composition of Ce-Al co-substituted zirconolite samples.

Substitution level, x	Fraction of zirconolite (wt.%)*	Ce speciation (%) (Ce^{3+}/Ce^{4+}, %)	Cation stoichiometry in zirconolite phase (f.u.)					
		Overall	Zirconolite#	Ca	Ce	Zr	Ti	Al
0.05	96.9(1)	26.4(8)/73.6(7)	19.5(8)/80.5(7)	0.98(7)	0.02(1)	1.00(10)	1.80(10)	0.24(5)
0.10	97.4(1)	23.2(6)/76.8(5)	19.2(6)/80.8(5)	0.93(6)	0.07(2)	1.02(6)	1.71(9)	0.33(6)
0.15	96.0(1)	31.3(5)/68.7(5)	29.0(5)/71.0(5)	0.86(7)	0.11(2)	1.06(10)	1.61(11)	0.39(6)
0.20	94.7(1)	36.4(6)/63.6(6)	34.6(6)/65.4(6)	0.82(5)	0.15(2)	0.98(6)	1.55(12)	0.57(6)
0.25	84.9(1)	42.8(4)/57.2(4)	39.1(4)/60.9(4)	0.75(6)	0.26(3)	0.92(6)	1.47(8)	0.66(8)
0.30	80.8(2)	38.8(3)/61.2(3)	33.0(3)/67.0(3)	0.78(6)	0.23(2)	0.90(9)	1.51(8)	0.59(6)
0.35	76.3(2)	40.5(2)/59.5(2)	31.6(2)/68.4(2)	0.68(6)	0.27(3)	1.03(8)	1.35(9)	0.71(8)

* Quantitative phase analysis based on Rietveld fits of PXRD results
\# Corrected by assuming the Ce in the impurity is trivalent;

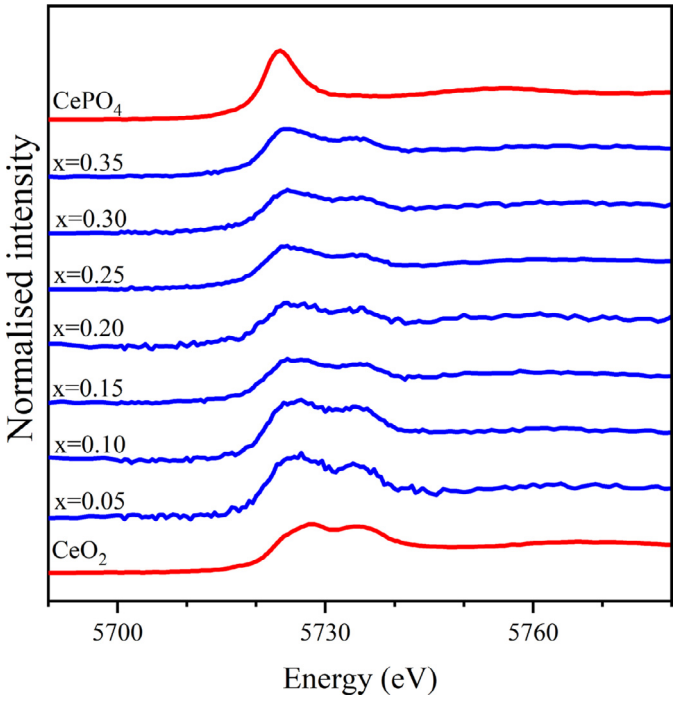

Fig. 6. Ce L_3 XANES data of $Ca_{1-x}Ce_xZrTi_{2-2x}Al_{2x}O_7$ and reference compounds of CeO_2 and $CePO_4$.

reduction of Ce^{4+} to Ce^{3+} was required to achieve the charge composition and to maintain overall charge neutrality. Consequently, Ce^{4+} was auto-reduced to Ce^{3+} and the overall ratio of Ce^{3+} to Ce^{4+} was increased. A similar reduction of Ce was observed when heat-treating $Ca_{1-x}Ce_xZrTi_{2-2x}Cr_{2x}O_7$ in air [26], although the unfavourable porous microstructure was observed in the sintered specimens.

Considering the chemical composition given in Table 2, the estimated formula show an increasing trend of Ce incorporation within the zirconolite phase. However, the actual Ce loadings were slightly lower than targeted, which was attributed to the existence of the secondary phases of perovskite (x = 0.05–0.15) and hibonite (x = 0.15–0.35) incorporating Ce. EDX analysis revealed that the Ca site was fully occupied in all cases, with the sum of Ca_{Ca} + Ce_{Ca} ≈ 1.0. Ce has a greater tendency toward auto reduction at high temperature, compared to Pu [27,28], this must therefore be taken into account when considering Pu^{4+} solubility within the $Ca_{1-x}Pu_xZrTi_{2-2x}Al_{2x}O_7$ system. The leaching rate of perovskite is also known to be higher than that of zirconolite [29], hence the formation of a Pu-bearing perovskite would be undesirable. For comparison, the leaching rate of Ca from Nd-hibonite (Nd was employed as analogue for trivalent actinide elements) was determined to be in the range 10^{-4} ~ 10^{-3} g•m^{-2}•d^{-1} in deionised water at 90 °C after 32 days [30]. This value was comparable to that reported in Nd-zirconolite (2.79×10^{-4} g•m^{-2}•d^{-1}, Ref. 31). This suggested hibonite might be a durable host for plutonium but required the detailed investigation. Compositional data obtained in this study suggests that the preferable formulation for CeO_2 is $Ca_{0.8}Ce_{0.2}ZrTi_{1.6}Al_{0.4}O_7$, as targeting this composition yielded the highest reasonable fraction of zirconolite at 94.7 wt.% without the

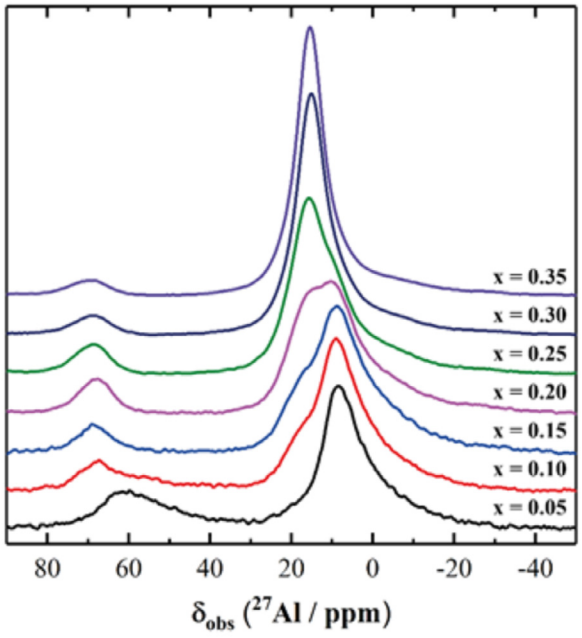

Fig. 7. ^{27}Al MAS NMR spectra (B_0 = 11.7 T, ν_R = 12.5 kHz) of $Ca_{1-x}Ce_xZrTi_{2-2x}Al_{2x}O_7$ samples.

presence of perovskite, which is representative of a PuO_2 incorporation rate of 14.86 wt.%. The actual Pu incorporation rate achievable may be lower for the $Ca_{1-x}Pu_xZrTi_{2-2x}Al_{2x}O_7$ system, given the lower tendency for auto reduction of Pu^{4+} to Pu^{3+} as a self-charge compensation mechanism when the solubility limit of Al^{3+} on the Ti^{4+} sites is reached.

Solid-state NMR spectroscopy probing ^{27}Al was used to resolve the local structure surrounding Al within the $Ca_{1-x}Ce_xZrTi_{2-2x}Al_{2x}O_7$ ceramics and to determine whether Al^{3+} substituted onto the octahedral Ti (I)/(III) sites or the trigonal bipyramidal Ti (II) site, shown schematically in Fig. 1. Solid-state NMR spectroscopy can resolve the local environment surrounding each atom via differences in the chemical shift (δ) which arise due differences in local coordination and consequent shielding effects experienced by the relevant nuclei. Furthermore, differences in the local electric field gradient surrounding the nuclei result in varying quadrupolar broadening effects, which are able to be observed in the spectra and provide information regarding the symmetry of the local electric field gradient. ^{27}Al MAS NMR spectra in Fig. 7 for the $Ca_{1-x}Ce_xZrTi_{2-2x}Al_{2x}O_7$ samples exhibit two broad, high intensity resonances with maximum intensities at δ_{obs} = 9 and 16 ppm, spanning from -25–25 ppm and 0–30 ppm, respectively, as well as a broad, lower intensity resonance with maximum intensity at either δ_{obs} = 62 ppm (x = 0.05) or δ_{obs} = 68 ppm (x = 0.10–0.35).

Quantitative phase analysis (as discussed above) identifies the presence of only zirconolite-2M and perovskite phases in the zirconolite samples with x = 0.05 and 0.10, hence any ^{27}Al MAS NMR resonances in the spectra for these samples must result from Al sites within the zirconolite-2M structure. Therefore, the presence of a resonance with maximum intensity at δ_{obs} = 62 ppm in the zirconolite samples where x = 0.05 and 0.10 is attributed to 5-coordinated Al species (Al^V) within the trigonal bipyramidal Ti(II) site. The large distribution of chemical shifts exhibited and asymmetric lineshape by this resonance are consistent with disorder of the Ti(II) sites. The resonance associated with the Al^V sites (between 62–68 ppm) had a significantly lower intensity when compared to the Al^{VI} sites in the zirconolite sample with x = 0.05, which is consistent with the relative bond strength in each site, with neutral 5-coordinated Ti-oxygen bond exhibiting the largest binding strength [32] and hence being less favourable toward substitution of Al^{3+}.

The high intensity resonances at δ_{obs} = 9 and 16 ppm were attributed to Al^{VI} sites within the zirconolite-2M structure and therefore indicate successful doping of Al^{3+} onto the Ti(I) and Ti(III) sites, forming $(Ti,Al)O_6$ octahedra. Considering the second coordination sphere of the Ti(I) and Ti(III) site in zirconolite-2M structure [22] and the differences in electronegativity of Ca and Zr atoms (χ = 1.0 and 1.4 for Ca and Zr, respectively), Al atoms occupying the Ti(III) sites would experience greater shielding and exhibit lower δ_{obs} than those occupying Ti(I) sites. The greater intensity at lower (more negative) chemical shifts in the broad octahedral resonance for the sample with x = 0.05 compared with that for the sample with x = 0.10, indicated that Al substituted for Ti in the Ti(III) site preferentially to the Ti(I) site, but as the Al doping level was increased, Al also substituted for Ti in the Ti(I) site. This shows that there is an effective limit on the extent of Al substitution possible on the Ti(III) site. This trend continues as the Al doping level is further increased (x = 0.15 – 0.35), and with an observed increase in the relative intensity of the ^{27}Al resonance for Al in the Ti(I) site compared to that of Al in the Ti(III) site.

In order to distinguish the contribution of hibonite the NMR spectra for the zirconolite samples with x = 0.15–0.35, ^{27}Al MAS NMR data for pure $CaAl_{12}O_{19}$ was also acquired (shown in Fig. S3 in *Supporting Information*). It was reported that hibonite contains Al in three distinct octahedrally coordinated sites (Al^{VI}) which resonate at δ_{iso} (isotropic chemical shift) = 22.3 ppm, 16.26 ppm and 9.92 ppm [33]. At fields below 18.8 T, these resonances overlap to a significant extent [34,35], such that only the resonances at δ_{iso} = 16.26 ppm and 9.92 ppm are clearly visible with the resonance at δ_{iso} = 22.3 ppm manifested as a shoulder on that at δ_{iso} =16.26 ± 0.05 ppm (shown in Fig. S3). The three Al^{VI} sites in hibonite will therefore contribute to the spectra presented here within the region of δ_{obs} at 16 ppm and 9 ppm, respectively [34,36]. This is consistent with the presence of a distinct shoulder at δ_{obs} = 16 ppm on the Al^{VI} resonance with maximum intensity at δ_{obs} = 9 ppm (Fig. S3). It is noteworthy that the ratio of intensities of the single Al^{IV} resonance and the three Al^{VI} resonances in the ^{27}Al MAS NMR spectrum of hibonite [34] are not consistent with that observed in the spectra presented here (which may be considered semi-quantitative due to the measured relaxation delay and non-selective pulse used during acquisition, even without determination of the quadrupolar parameters and simulation of the spectra). This, and the observation of an additional shoulder on the main octahedral resonance at δ_{obs} = - 3pm, indicates that the broad octahedral resonance contains dominant contributions from resonances due to multiple additional octahedral sites which overlap with those present in hibonite.

Al_2O_3 contains a single octahedral Al site that resonates at δ_{obs} = 13.5 ppm [37], and may contribute to the NMR data for the zirconolite samples with x = 0.25–0.35. The small amount of Al_2O_3 in these samples (1.6–7.4 mol. %), however, is not sufficient to account for all of the intensity in the Al^{VI} region of the spectra for these compositions, again indicating contributions from resonances due to multiple additional octahedral sites which overlap with those present in both hibonite and Al_2O_3. Together, the ^{27}Al NMR data for all compositions shows that for all doping levels investigated Al substitutes into both Ti^V and Ti^{VI} coordinated sites, with a strong preference for substituting onto Ti^{VI} coordinated sites. In regard to substitution in Ti^{VI} sites, at low doping levels, Al substitutes for Ti in the Ti(III) site preferentially to the Ti(I) site; but as the Al doping level was increased beyond x = 0.05, Al then substitutes for Ti in the Ti(I) site. This suggests that the

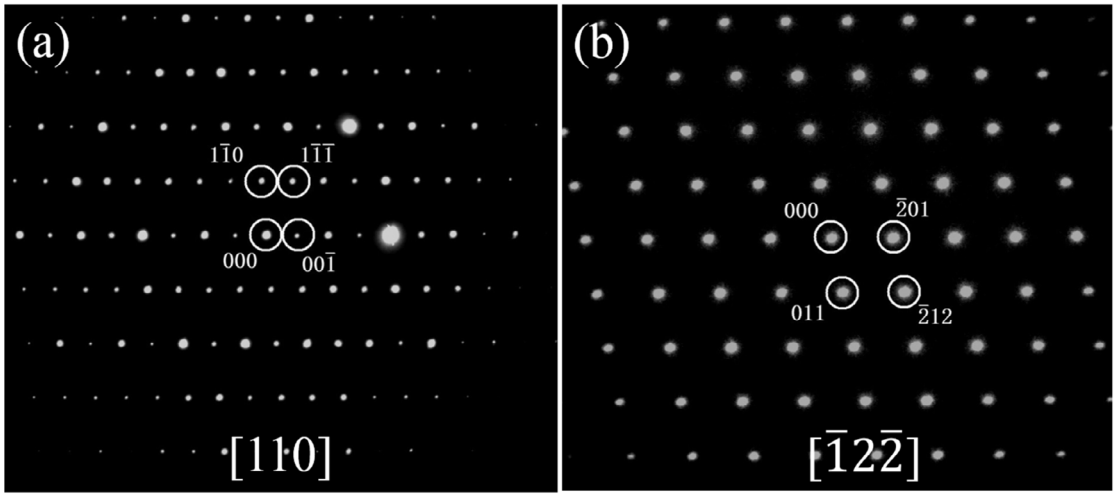

Fig. 8. Zone axis electron diffraction patterns for $Ca_{0.75}Ce_{0.25}ZrTi_{1.5}Al_{0.5}O_7$ composition, indexed in C2/*c* space group as zirconolite-2M. [110] zone axis shown left (a), and [$\bar{1}2\bar{2}$] zone axis on right (b).

limit on the extent of Al substitution possible on the Ti(III) site is reached at $x \approx 0.05$.

Intergrowth defects in zirconolite structures are commonly observed, giving rise to variations in the stacking relationship between adjacent hexagonal bronze type structural modules. The occurrence of these observed polytypes and intergrowth defects is known to depend on the targeted chemical composition, and even a small concentration of dopant species (particularly rare earth cations) may be sufficient to result in complex intergrowth defects that are not readily detectable using X-ray powder diffraction techniques. However, such intergrowth defects are readily evidenced in zone axis electron diffraction patterns by characteristic streaking associated with structural disorder in the corresponding real space direction. Vance *et al.* observed that extensive twinning, stacking disorder and other polytype intergrowths existed in uranium doped zirconolite (nominal $CaU_{0.2}Zr_{0.8}Ti_2O_7$) [38]. Moreover, it was reported that Al-Nd co-doped zirconolite derived from glass-ceramic exhibited heavy stacking faults [39]. The zone axis electron diffraction patterns of the $x = 0.25$ composition, shown in Fig. 8, are indexed in the C2/*c* space group for the zirconolite-2M structure. No evidence of streaking is apparent, demonstrating the absence of significant twinning or stacking disorder. This also demonstrates that zirconolite was present only as the 2M polytype, consistent with indexed PXRD data.

4. Conclusion

Ce-Al co-doped zirconolite ceramics consistent with $Ca_{1-x}Ce_xZrTi_{2-2x}Al_{2x}O_7$ stoichiometry were fabricated by sintering at 1450°C in air. It was revealed that the existence of zirconolite-2M as the dominant crystalline phase. The composition and weight fraction of accompanying secondary phases were dependent on the level of targeted Ce incorporation. Perovskite was present (albeit at low concentrations) for compositions for which $x \leq 0.15$, after which further Ce incorporation appeared to stabilise hibonite and alumina as accessory phases, the relative weight fraction of which tends to increase with raised levels of Ce-doping. It was hypothesised that the solubility limit site was reached between $x = 0.15$–0.20, allowing excess Ce/Al to react with perovskite to form hibonite and residual Al_2O_3. Al^{3+} occupied both 6-fold Ti(I) and Ti(III) sites, with preferential occupation of Ti(III) sites, and Ce underwent partial reduction to Ce^{3+}. The variations in redox behaviour concerning Ce and Pu should be considered for final Pu-bearing wasteforms. The most favourable phase assemblage with a high zirconolite yield and a high incorporation rate of CeO_2 was produced for the target stoichiometry $Ca_{0.80}Ce_{0.20}ZrTi_{1.60}Al_{0.40}O_7$. Overall, these results are promising for progress towards a suitable host phase assemblage for stockpiled plutonium.

Declaration of Competing Interest

The authors declare that they have **no** known competing financial interests or personal relationships that could have appeared to influence the work reported in this paper.

CRediT authorship contribution statement

Min-Xiao Zhong: Conceptualization, Formal analysis, Writing – review & editing. **Brant Walkley:** Methodology, Formal analysis, Writing – review & editing. **Daniel J. Bailey:** Formal analysis, Writing – review & editing. **Lewis R. Blackburn:** Methodology, Formal analysis, Writing – review & editing. **Hao Ding:** Formal analysis, Writing – review & editing. **Shi-Qian Wang:** Methodology, Writing – review & editing. **Wei-Chao Bao:** Formal analysis, Writing – review & editing. **Laura J. Gardner:** Formal analysis, Writing – review & editing. **Shi-Kuan Sun:** Conceptualization, Supervision, Writing – original draft, Writing – review & editing. **Martin C. Stennett:** Formal analysis, Writing – review & editing. **Claire L. Corkhill:** Formal analysis, Writing – review & editing. **Neil C. Hyatt:** Supervision, Writing – review & editing.

Acknowledgement

MXZ appreciates the China Scholarship Council, Nuclear Power Institute of China for financial support. LRB, NCH, CLC, SKS and LJG are grateful for financial support from the Nuclear Decommissioning Authority and EPSRC under Grant No. EP/L014041/1, EP/S01019X/1, EP/N017374/1, EP/M026566/1 and EP/R511754/1. SKS acknowledge Science and Technology Program of Guangzhou for funding under Grant No. 201704030095. This research utilised the HADES/MIDAS facility at the University of Sheffield established with financial support from EPSRC and BEIS, under Grant EP/T011424/1 [40]. We wish to thank and acknowledge Dr Sandra van Meurs, Department of Chemistry, University of Sheffield, for assistance in acquiring the NMR data.

Supplementary materials

Supplementary material associated with this article can be found, in the online version, at doi:10.1016/j.jnucmat.2021.153198.

References

[1] NC. Hyatt, Plutonium management policy in the United Kingdom: the need for a dual track strategy, Energy Policy 101 (2017) 303–309.
[2] Nuclear Decommissioning Authority (NDA). Plutonium topic strategy: credible options technical analysis. 2009.
[3] W.J. Bourcier, K. Sickafus, Storing Waste in Ceramic, Uncertainty Underground: Yucca Mountain and the Nation's High-Level Nuclear Waste, MIT Press, Cambridge, 2006.
[4] K.P. Hart, Y. Zhang, E. Loi, Z. Aly, M.W.A. Stewart, A. Brownscombe, B.B. Ebbinghaus, W. Bourcier, Aqueous durability of titanate ceramics designed to immobilize excess plutonium, MRS Proc. 608 (1999) 353.
[5] S.V. Yudintsev, S.V. Stefanovsky, R.C. Ewing, S.V. Krivovichev, P.C. Burns, I.G. Tananaev, Chapter 13 - actinide host phases as radioactive waste forms, in: Structural Chemistry of Inorganic Actinide Compounds, Elsevier, Amsterdam, 2007, pp. 457–490.
[6] RC. Ewing, Ceramic matrices for plutonium disposition, Prog. Nucl. Energy 49 (8) (2007) 635–643.
[7] R.C. Ewing, TJ. Headley, Alpha-recoil damage in natural zirconolite ($CaZrTi_2O_7$), J. Nucl. Mater. 119 (1) (1983) 102–109.
[8] G.R. Lumpkin, K.R. Whittle, C.J. Howard, Z. Zhang, F.J. Berry, G. Oates, C.T. Williams, AN. Zaitsev, Crystal chemistry and cation ordering in zirconolite 2M, MRS Online Proc. Libr. 932 (1) (2006) 531.
[9] D.S. Perera, B.D. Begg, E.R. Vance, M.W.A. Stewart, Application of crystal chemistry in the development of radioactive wasteforms, J. Mater. Online 1 (2005) 1–7.
[10] B.M. Gatehouse, I.E. Grey, R.J. Hill, H.J. Rossell, Zirconolite, $CaZr_xTi_{3-x}O_7$; structure refinements for near-end-member compositions with x = 0.85 and 1.30, Acta Crystallogr. B 37 (1981) 306–312.
[11] K.R. Whittle, K.L. Smith, N.C. Hyatt, GR. Lumpkin, Neutron and resonant X-ray diffraction studies of zirconolite-2M, MRS Proc. 1107 (2008) 331.
[12] B.D. Begg, E.R. Vance, SD. Conradson, The incorporation of plutonium and neptunium in zirconolite and perovskite, J. Alloys Compd. 271–273 (1998) 221–226.
[13] P.A. Bingham, R.J. Hand, M.C. Stennett, N.C. Hyatt, MT. Harrison, The use of surrogates in waste immobilization studies: a case study of plutonium, MRS Proc. 1107 (2008) 421.
[14] L.R. Blackburn, S. Sun, L.J. Gardner, E.R. Maddrell, M.C. Stennett, NC. Hyatt, A systematic investigation of the phase assemblage and microstructure of the zirconolite $CaZr_{1-x}Ce_xTi_2O_7$ system, J. Nucl. Mater. 535 (2020) 152137.
[15] E.R. Vance, C.J. Ball, R.A. Day, K.L. Smith, M.G. Blackford, B.D. Begg, PJ. Angel, Actinide and rare earth incorporation into zirconolite, J. Alloys Compd. 213-214 (1994) 406–409.
[16] Nuclear Decommissioning Authority (NDA). Direct research portfolio annual report 2018 to 2019. 2020.
[17] B. Toby, EXPGUI, a graphical user interface for GSAS, J. Appl. Crystallogr. 34 (2) (2001) 210–213.
[18] G.T. Seidler, D.R. Mortensen, A.J. Remesnik, J.I. Pacold, N.A. Ball, N. Barry, M. Styczinski, OR. Hoidn, A laboratory-based hard x-ray monochromator for high-resolution x-ray emission spectroscopy and x-ray absorption near edge structure measurements, Rev. Sci. Instrum. 85 (11) (2014) 113906.
[19] E.P. Jahrman, W.M. Holden, A.S. Ditter, D.R. Mortensen, G.T. Seidler, T.T. Fister, S.A. Kozimor, L.F.J. Piper, J. Rana, N.C. Hyatt, M.C. Stennett, An improved laboratory-based x-ray absorption fine structure and x-ray emission spectrometer for analytical applications in materials chemistry research, Rev. Sci. Instrum. 90 (2) (2019) 024106.
[20] L.M. Mottram, S. Cafferkey, A.R. Mason, T. Oulton, S.-K. Sun, D.J. Bailey, M.C. Stennett, NC. Hyatt, A feasibility investigation of speciation by Fe K-edge XANES using a laboratory X-ray absorption spectrometer, J. Geosci. 65 (1) (2020) 27–35.
[21] B. Ravel, M.A Newville, ARTEMIS, HEPHAESTUS: data analysis for X-ray absorption spectroscopy using IFEFFIT, J. Synchrotron Radiat. 12 (4) (2005) 537–541.
[22] K.R. Whittle, N.C. Hyatt, K.L. Smith, I. Margiolaki, F.J. Berry, K.S. Knight, GR. Lumpkin, Combined neutron and X-ray diffraction determination of disorder in doped zirconolite-2M, Am. Mineral. 97 (2–3) (2012) 291–298.
[23] J. Li, A. Medina Elena, K. Stalick Judith, W. Sleight Arthur, M.A. Subramanian, Structural studies of $CaAl_{12}O_{19}$, $SrAl_{12}O_{19}$, $La_{2/3+\delta}Al_{12-\delta}O_{19}$, and $CaAl_{10}NiTiO_{19}$ with the hibonite structure; indications of an unusual type of ferroelectricity, Z. Naturforsch. B 71 (2016) 475–484.
[24] H.S. Jeon, S.K. Kim, S.C. Kim, S.H. Park, H.L.SI. Park, Mho Indirect energy transfer of Ce3+→Eu2+ in CaAl12O19 phosphor, Solid State Commun 102 (7) (1997) 555–559.
[25] D. Makovec, D. Kolar, Internal oxidation of Ce^{3+}-$BaTiO_3$ solid solutions, J. Am. Ceram. Soc. 80 (1) (1997) 45–52.
[26] L.R. Blackburn, S.-K. Sun, S.M. Lawson, L.J. Gardner, H. Ding, C.L. Corkhill, E.R. Maddrell, M.C. Stennett, NC. Hyatt, Synthesis and characterisation of $Ca_{1-x}Ce_xZrTi_{2-2x}Cr_{2x}O_7$: analogue zirconolite wasteform for the immobilisation of stockpiled UK plutonium, J. Eur. Ceram. Soc. 40 (15) (2020) 5909–5919.
[27] M. Zamoryanskaya, B. Burakov, Feasibility limits in using cerium as a surrogate for plutonium incorporation in zircon, zirconia and pyrochlore, Mater. Res. Soc. Symp. Proc. 663 (2000) 301–307.
[28] C. Lopez, X. Deschanels, J.M. Bart, J.M. Boubals, C. Den Auwer, E. Simoni, Solubility of actinide surrogates in nuclear glasses, J. Nucl. Mater. 312 (1) (2003) 76–80.
[29] W. Lutze, RC. Ewing, Radioactive Waste Forms for the Future, North Holland Physics Publishing, New York, 1988.
[30] I. Hayakawa, H. Kamizono, Leaching of Al_2O_3-based nuclear waste forms, J. Nucl. Sci. Technol. 30 (1993) 673–679.
[31] X. Cai, Y.C. Teng, L. Wu, K.B. Zhang, Y. Huang, The synthesis and chemical durability of Nd-doped single-phase zirconolite solid solutions, J. Nucl. Mater. 479 (2016) 455–460.
[32] J. Mulroute, DM. Duffy, Ab initio study of the effect of charge localisation on the properties of defects in magnesium oxide and zirconolite, R. Soc. Proc. 467 (2011) 2054–2065 A.
[33] L.-S. Du, JF. Stebbins, Calcium and strontium hexaluminates: NMR evidence that "Pentacoordinate" cation sites are four-coordinated, J. Phys. Chem. B 108 (2004) 3681–3685.
[34] D. Müller, W. Gessner, A. Samoson, E. Lippmaa, G. Scheler, Solid-state ^{27}Al NMR studies on polycrystalline aluminates of the system CaO-Al_2O_3, Polyhedron 5 (1986) 779–785.
[35] S.R. Jansen, H.T. Hintzen, R. Metselaar, J.W. de Haan, L.J.M. van de Ven, A.P.M. Kentgens, GH. Nachtegaal, Multiple quantum ^{27}Al magic-angle-spinning nuclear magnetic resonance spectroscopic study of $SrAl_{12}O_{19}$: identification of a ^{27}Al resonance from a well-defined AlO_5 site, J. Phys. Chem. B 102 (1998) 5969–5976.
[36] C. Gervais, K.J.D. MacKenzie, ME. Smith, Multiple magnetic field ^{27}Al solid-state NMR study of the calcium aluminates $CaAl_4O_7$ and $CaAl_{12}O_{19}$, Magn. Reson. Chem. 39 (2001) 23–28.
[37] L.A. O'Dell, S.L.P. Savin, A.V. Chadwick, ME. Smith, A ^{27}Al MAS NMR study of a sol–gel produced alumina: identification of the NMR parameters of the θ-Al_2O_3 transition alumina phase, Solid State Nucl. Magn. Reson. 31 (2007) 169–173.
[38] E.R. Vance, G.R. Lumpkin, M.L. Carter, D.J. Cassidy, C.J. Ball, R.A. Day, BD. Begg, Incorporation of uranium in zirconolite ($CaZrTi_2O_7$), J. Am. Ceram. Soc. 85 (7) (2002) 1853–1859.
[39] C..Z. Liao, K. Shih, WE. Lee, Crystal structures of Al–Nd codoped zirconolite derived from glass matrix and powder sintering, Inorg. Chem. 54 (15) (2015) 7353–7361.
[40] N.C. Hyatt, C.L. Corkhill, M.C. Stennett, R.J. Hand, L.J. Gardner, CL. Thorpe, The HADES facility for high activity decommissioning engineering & science: part of the UK national nuclear user facility, IOP Conf. Ser. Mater. Sci. Eng. 818 (2020) 012022.